J. Fluid Mech. (2009), *vol.* 621, *pp.* 131–154.
doi:10.1017/S0022112008004795 Printed in the United Kingdom

Stability analysis of cusped bubbles in viscoelastic flows

R. YOU[1], A. BORHAN[2] AND H. HAJ-HARIRI[1]†

[1]Department of Mechanical and Aerospace Engineering, University of Virginia, Charlottesville, VA 22904, USA

[2]Department of Chemical Engineering, The Pennsylvania State University, University Park, PA 16802, USA

(Received 22 June 2007 and in revised form 10 October 2008)

Experiments have established that an axisymmetric sharp trailing edge of a gas bubble in a viscoelastic fluid can develop into a three-dimensional 'knifelike' shape under certain conditions (high capillary number, large bubble size). A numerical study is conducted to discover the physics of this phenomenon. The axisymmetric deformation of a bubble rising buoyantly in a viscoelastic fluid is simulated by solving the axisymmetric flow equations coupled with the constitutive equations of the finitely extensible nonlinear elastic Chilcott–Rallison (FENE-CR) model. The three-dimensional temporal linear stability analysis of this axisymmetric base state is carried out. The dominant eigenvalue which is indicative of the growth rate of the perturbations is computed. The only unstable eigenmode has azimuthal wavenumber m equal to 2. The corresponding eigenfunction shows that indeed a sharp axisymmetric tail develops a knife-edge form. A further investigation of the energy budget of the disturbances for $m = 2$ is performed to determine the production and dissipation terms affecting the growth of this instability. It is shown that the normal gradient of the base-state pressure along the free surface plays an important role in the evolution of the instability.

1. Introduction

It has been observed in experimental studies (Hassager 1979; Liu, Liao & Joseph 1995) that an asymmetric cusplike tip would abruptly appear at the trailing edge of a buoyantly-rising gas bubble in a viscoelastic fluid under certain conditions. In this study, the term cusp is used to indicate an apparent singularity of the outer solution in the sense of singular perturbation. The finite surface tension will of course ameliorate this singularity in the inner solution, thus disallowing a true cusp. Although all geometric and physical conditions prompt an axisymmetric shape to appear, under certain conditions, a three-dimensional cusp can form at the rear tip of a bubble. Close observation of the cusped tip reveals a broad edge in one direction and a sharp edge in the perpendicular direction. This knifelike tip is dramatically different from the symmetric bubble observed in a Newtonian fluid under normally identical conditions. Based on experiments, Liu *et al.* (1995) suggested that the formation of such knife-like cusp is related to the capillary number *Ca*. Their results indicated the cusped bubble tail abruptly forms with *Ca* near unity. They also observed that

† Email address for correspondence: hh2b@virginia.edu

the bubble volume increase above a critical value leads to the formation of a cusped tail and discontinuity of the rising velocity. Belmonte (2000) experimentally observed that, above some critical volume, a buoyancy-driven bubble in a wormlike micellar solution experiences shape oscillations in time between an axisymmetrically cusped tip and a snap-back round tip which are accompanied by an abrupt discontinuity in bubble-rising velocity with respect to bubble volume.

The fast-growing computational power makes linear stability analysis an affordable technique to tackle hydrodynamic stability problems of complicated base flows. Zebib (1987) presented a technique to effectively remove spurious eigenvalues in solving linear stability problems by spectral method. Kim & Pearlstein (1990) conducted a stability study of the flow past a sphere. They used spectral method to compute the steady axisymmetric flow as the base state and then perturbed it with small disturbances of axisymmetric and non-axisymmetric modes. Their calculations showed that the base flow is stable for axisymmetric perturbations for $Re \leqslant 190$ but undergoes a Hopf bifurcation at $Re = 175.1$ for perturbations with azimuthal wavenumber equal to unity. Kuhlmann & Rath (1993) investigated the stability of steady axisymmetric thermocapillary flow in a cylindrical liquid bridge. The base state and three-dimensional perturbations were solved by the spectral method. Their linear stability results identified the mode for azimuthal wavenumber equal to one as the critical mode. The disturbance for the unstable mode is either steady or oscillatory, depending on the Prandtl number. Ramanan & Homsy (1994) made a numerical investigation of the stability of classical lid-driven cavity flow. The critical Reynolds number and the critical wavelength of the neutral mode were identified in their calculations. The mechanism of instability was analysed through energy budget calculations and indicated a Goertler-type instability. The linear stability of the steady thermocapillary flow inside a cylindrical liquid bridge was studied by Levenstam, Amberg & Winkler (2001). The base state was computed using finite element method. The linear stability analysis revealed that the axisymmetric base state is more stable at intermediate than high or low Prandtl numbers due to the stabilizing effect of thermocapillary forces.

In the present study, the numerical analysis of the cusped shape is conducted by combining computational fluid dynamics (CFD) and linear stability analysis. An axisymmetrically cusped basic state is first established using CFD. Then a linear stability analysis is carried out to predict the onset of an asymmetric cusp above critical conditions. Finally, the mechanism of cusp formation is explored by performing energy budget analysis. In § 2, the physical problem is described, and the relevant parameters are defined. In §§ 3 and 4, the formulations of governing equations and boundary conditions for base flow and perturbations are presented, respectively. The CFD results of base-state flow is discussed in § 5. The linear stability analysis results and the exploration of the instability mechanism are presented in §§ 6 and 7 summarizes the main results of this paper.

2. Problem Description

2.1. *Physical problem*

The physical problem is modelled as a gas bubble rising buoyantly along the centreline of an open-ended vertical tube filled with an initially quiescent finitely extensible nonlinear elastic Chilcott–Rallison (FENE-CR; Chilcott & Rallison 1988) model fluid, as shown in figure 1. The diameter of the tube D_t is set 10 times larger than the diameter of a spherical bubble D. We assume that the gas bubble has sufficiently

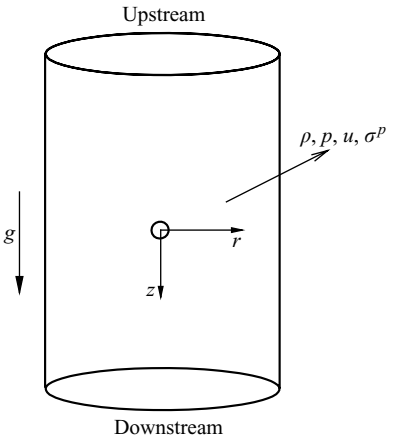

FIGURE 1. Sketch of a bubble suspended in a vertical tube filled with a viscoelastic fluid.

small density and viscosity compared with those of the exterior phase fluid so that the stress field inside the bubble is neglected. It is assumed that the surface tension γ is uniform. Also, thermal effects are not considered in this study. The initially spherical bubble rising up and deforming during transient states is simulated in a reference frame attached to the bubble centre. Under certain conditions, the bubble can develop a three-dimensional trailing edge. We perform linear stability analysis to show this unusual feature.

2.2. *Non-dimensionalization*

The characteristic quantities used for non-dimensionalization are the initially spherical bubble diameter D, exterior phase density ρ, exterior fluid solvent viscosity μ_s, polymeric viscosity μ_p, bubble surface tension γ and polymer relaxation time λ. The expressions

$$U^* = \frac{\rho g D^2}{\mu_s}, \quad T^* = \frac{D}{U^*}, \quad P^* = \rho U^{*2}, \quad \sigma^{p*} = \frac{\mu_p U^*}{D}$$

denote the characteristic velocity, time, pressure and polymer stress, respectively. The dimensionless parameters are defined as

$$Re = \frac{\rho U^* D}{\mu_s}, \quad c = \frac{\mu_p}{\mu_s}, \quad Ca = \frac{\mu_s U^*}{\gamma}, \quad De = \frac{\lambda U^*}{D}$$

for Reynolds number, the ratio of the polymer contribution to the viscosity to the solvent viscosity, capillary number and Deborah number, respectively.

In the result §§ 5 and 6, the definitions of Reynolds, capillary and Deborah numbers are based on the bubble terminal velocity U_T^* and total viscosity of the exterior phase $\mu_s + \mu_p$ instead of U^* and μ_s. As such, they are identified by the subscript T: Re_T, Ca_T and De_T. In our computations, the unsubscripted parameters are set to given values. The values of the subscripted parameters are not known *a priori* and are obtained as a part of the solution. When comparing with experimental results, the latter set is more relevant. Depending on the actual Reynolds number, $U^*/U_T^* \sim O(1\text{–}100)$.

3. Base-state formulation

3.1. *Governing equations*

The dimensionless flow equations of the exterior bulk phase are

$$\nabla \cdot \boldsymbol{u} = 0, \tag{3.1}$$

$$\frac{\partial \boldsymbol{u}}{\partial t} + \nabla \cdot (\boldsymbol{u}\boldsymbol{u}) = -\nabla P + \frac{1}{Re}\nabla^2 \boldsymbol{u} + \frac{c}{Re}\nabla \cdot \sigma^p. \tag{3.2}$$

In the momentum equation, the hydrostatic pressure is absorbed in the modified pressure P. The viscoelastic effect is represented by the polymer stress tensor σ^p, which is calculated from the constitutive equations of the FENE-CR model (Chilcott & Rallison 1988):

$$\sigma^p = \frac{f(R)(\boldsymbol{A} + \boldsymbol{I})}{De}, \tag{3.3}$$

$$\overset{\triangledown}{\boldsymbol{A}} + \frac{f(R)}{De}\boldsymbol{A} = \nabla \boldsymbol{u} + (\nabla \boldsymbol{u})^T, \tag{3.4}$$

$$\overset{\triangledown}{\boldsymbol{A}} \equiv \frac{\partial \boldsymbol{A}}{\partial t} + \boldsymbol{u} \cdot \nabla \boldsymbol{A} - \boldsymbol{A} \cdot \nabla \boldsymbol{u} - (\nabla \boldsymbol{u})^T \cdot \boldsymbol{A}, \tag{3.5}$$

in which $\boldsymbol{A}$ represents an ensemble average of the dyadic product $\boldsymbol{R}\boldsymbol{R}$ of the 'FENE dumbbell' end-to-end vector $\boldsymbol{R}$. The effect of fluid finite extensibility is enforced by the nonlinear function $f(R)$ which takes the following form:

$$f(R) = \frac{1}{1 - tr(\boldsymbol{A} + \boldsymbol{I})/L^2}.$$

Here, the specified parameter L denotes the ratio of the length of a fully extended dumbbell to its equilibrium length. The complete formulation of the above-given governing equations in cylindrical coordinates is described in the Appendix.

3.2. *Boundary conditions*

The boundary conditions on the free surface consist of dynamic and kinematic conditions. By assuming flow axisymmetry, the dimensionless dynamic conditions in locally orthogonal coordinates are given as

$$P + \frac{Z_s}{Re} - \frac{2}{Re}\frac{\partial u_n}{\partial n} + \frac{K}{ReCa} - \frac{c}{Re}\sigma^p_{nn} = 0 \tag{3.6}$$

for normal stress balance and

$$\frac{\partial u_n}{\partial s} + \frac{\partial u_s}{\partial n} + c\sigma^p_{ns} = 0 \tag{3.7}$$

for tangential stress balance. Here, n and s denote the local coordinates normal and tangential to the bubble surface; n is defined positive when pointing to the exterior fluid; Z_s denotes the axial position of a bubble surface point relative to the bubble centre. The curvature K in the axisymmetric case is

$$K = \frac{\partial n_z}{\partial z} + \frac{\partial n_r}{\partial r} + \frac{n_r}{r}. \tag{3.8}$$

The dimensionless kinematic condition states that there is no flow across the free surface, i.e.

$$\frac{\partial H_n}{\partial t} + u_s \frac{\partial H_n}{\partial s} = u_n. \tag{3.9}$$

Along the far-field outer boundary, $\boldsymbol{u} = -U_T \hat{\boldsymbol{e}}_z$ is imposed, where U_T denotes instantaneous bubble migration velocity. The no-slip and no-penetration conditions are imposed along the sidewall. Symmetry condition is imposed along the axis of symmetry. For the polymer stretch tensor $\boldsymbol{A}$, as (3.4) is hyperbolic in time, $\boldsymbol{A} = 0$ is required on the upstream boundary.

3.3. *Outline of the computational method*

The finite volume method is used to discretize the above system of equations and boundary conditions in boundary-fitted coordinates. The introduction of an artificial compressibility factor (Chorin 1967) in the continuity equation effectively increases the convergence rate of the computations by directly coupling the pressure and velocity fields. The flux-difference splitting scheme (Roe 1981) is adopted to effectively overcome numerical instability associated with the change of type in the governing equations, especially for highly elastic fluids. The application of this combination of techniques to viscoelastic flow problems is novel. The methods have their root in high-speed aerodynamics in which change of type between elliptic (subsonic) and hyperbolic (supersonic) is common and needs to be handled automatically. This very same capability was needed (and missing) in handling viscoelastic flow simulations. The implementation of free-surface boundary conditions on the boundary-fitted grid enables the solver to simulate immiscible two-phase flows with high fidelity for resolving the moving interface. A complete description of the numerical implementation of the governing equations and boundary conditions is presented by You, Borhan & Haj-Hariri (2008).

4. Perturbed-state formulation

4.1. *Governing equations*

Once the axisymmetric steady-state basic flow is obtained, we perform a linear stability analysis of three-dimensional small disturbances introduced to the base-state solution. The system of three-dimensional equations involves 11 variables that include the pressure (P), 3 velocity components in the axial, radial and azimuthal directions (u_z, u_r, u_ϕ), 6 components of the polymer stretch tensor ($A_{zz}, A_{rr}, A_{zr}, A_{\phi\phi}, A_{z\phi}, A_{r\phi}$) and the small displacement normal to the bubble surface (H_n). Each variable q can be decomposed into a basic state term (denoted by $\bar{q}$) and a three-dimensional perturbation (denoted by q') as shown below:

$$q(z, r, \phi, t) = \bar{q}(z, r) + q'(z, r, \phi, t). \tag{4.1}$$

The basic state is obtained from the CFD solution. For a steady base flow solution, the base-state variables are collectively denoted by a vector $\bar{\boldsymbol{Q}}$ as

$$\bar{\boldsymbol{Q}}(z, r) = \begin{bmatrix} \bar{P} \\ \bar{\boldsymbol{u}} \\ \bar{\boldsymbol{A}} \\ \bar{H}_n \end{bmatrix} (z, r), \tag{4.2}$$

$$\bar{\boldsymbol{u}} = [\bar{u}_z, \bar{u}_r, 0]^T, \tag{4.3}$$

$$\bar{\boldsymbol{A}} = [\bar{A}_{zz}, \bar{A}_{rr}, \bar{A}_{zr}, \bar{A}_{\phi\phi}, 0, 0]^T, \tag{4.4}$$

$$\bar{H}_n = 0. \tag{4.5}$$

The corresponding three-dimensional perturbation terms are assumed, without loss of generality, to be of the form

$$\boldsymbol{Q}'(z, r, \phi, t) = \begin{bmatrix} P' \\ u'_z \\ u'_r \\ u'_\phi \\ A'_{zz} \\ A'_{rr} \\ A'_{zr} \\ A'_{\phi\phi} \\ A'_{z\phi} \\ A'_{r\phi} \\ H'_n \end{bmatrix} \quad (z, r, \phi, t) = \begin{bmatrix} \tilde{P}(z, r)\cos(m\phi) \\ \tilde{u}_z(z, r)\cos(m\phi) \\ \tilde{u}_r(z, r)\cos(m\phi) \\ \tilde{u}_\phi(z, r)\sin(m\phi) \\ \tilde{A}_{zz}(z, r)\cos(m\phi) \\ \tilde{A}_{rr}(z, r)\cos(m\phi) \\ \tilde{A}_{zr}(z, r)\cos(m\phi) \\ \tilde{A}_{\phi\phi}(z, r)\cos(m\phi) \\ \tilde{A}_{z\phi}(z, r)\sin(m\phi) \\ \tilde{A}_{r\phi}(z, r)\sin(m\phi) \\ \tilde{H}_n(z, r)\cos(m\phi) \end{bmatrix} e^{\omega t}, \tag{4.6}$$

where the real number m is the azimuthal wavenumber and ω is the complex growth rate which is to be determined in an eigenvalue problem. The real part of ω represents the growth rate of disturbances, and the imaginary part represents the frequency of disturbances oscillating in time.

By substituting decompositions of the form (4.1) into flow equations (3.1), (3.2) and the FENE-CR model equations (3.3)–(3.5), linearizing them and subtracting the basic state solutions, the equations governing small disturbances read

$$\nabla \cdot \boldsymbol{u}' = 0, \tag{4.7}$$

$$\frac{\partial \boldsymbol{u}'}{\partial t} + \bar{\boldsymbol{u}} \cdot \nabla \boldsymbol{u}' + \boldsymbol{u}' \cdot \nabla \bar{\boldsymbol{u}} = -\nabla P' + \frac{1}{Re}\nabla^2 \boldsymbol{u}' + \frac{c}{Re}\nabla \cdot \sigma^{p'}, \tag{4.8}$$

$$\overset{\triangledown}{\boldsymbol{A}}' + \frac{f(\bar{R})}{De}\boldsymbol{A}' + \frac{f(R)'}{De}\bar{\boldsymbol{A}} = \nabla \boldsymbol{u}' + (\nabla \boldsymbol{u}')^T, \tag{4.9}$$

$$\overset{\triangledown}{\boldsymbol{A}}' = \frac{\partial \boldsymbol{A}'}{\partial t} + \boldsymbol{u}' \cdot \nabla \bar{\boldsymbol{A}} + \bar{\boldsymbol{u}} \cdot \nabla \boldsymbol{A}' - \boldsymbol{A}' \cdot \nabla \bar{\boldsymbol{u}} - \bar{\boldsymbol{A}} \cdot \nabla \boldsymbol{u}' - (\nabla \boldsymbol{u}')^T \cdot \bar{\boldsymbol{A}} - (\nabla \bar{\boldsymbol{u}})^T \cdot \boldsymbol{A}', \tag{4.10}$$

$$\sigma^{p'} = \frac{f(\bar{R})\boldsymbol{A}'}{De} + \frac{f(R)'(\bar{\boldsymbol{A}} + I)}{De}. \tag{4.11}$$

In (4.9) and (4.11), $f(R)' = (f(\bar{R})^2/L^2)tr(\boldsymbol{A}')$. The complete formulation of the perturbed governing equations in cylindrical coordinates is presented in the Appendix.

By inserting the form (4.6) for $\boldsymbol{Q}'$, the governing equations for the perturbations (4.7)–(4.11) can be cast into a matrix equation:

$$\boldsymbol{A}_d \tilde{\boldsymbol{X}}_d = -\boldsymbol{\omega} \boldsymbol{B}_d \tilde{\boldsymbol{X}}_d, \tag{4.12}$$

where

$$\tilde{\boldsymbol{X}}_d = \begin{bmatrix} \tilde{P} \\ \tilde{\boldsymbol{u}} \\ \tilde{\boldsymbol{A}} \end{bmatrix} (z, r), \tag{4.13}$$

$$\tilde{\boldsymbol{u}} = [\tilde{u}_z, \tilde{u}_r, \tilde{u}_\phi]^T, \tag{4.14}$$

$$\tilde{\boldsymbol{A}} = [\tilde{A}_{zz}, \tilde{A}_{rr}, \tilde{A}_{zr}, \tilde{A}_{\phi\phi}, \tilde{A}_{z\phi}, \tilde{A}_{z\phi}]^T. \tag{4.15}$$

In the above, $\tilde{\boldsymbol{X}}_d$ is the eigenfunction and ω is the eigenvalue of the system. The matrices in (4.12) are given below. In particular, $\boldsymbol{A}_d$ is an operator:

$$\boldsymbol{A}_{\mathrm{d}} = \begin{bmatrix}
0 & \frac{\partial}{\partial z} & \frac{\partial}{\partial r}+\frac{1}{r} & \frac{m}{r} & 0 & 0 & 0 & 0 & 0 & 0 \\
\frac{\partial}{\partial z} & M_1 & \frac{\partial \bar{u}_z}{\partial r} & 0 & M_{19}+M_{25} & M_{25} & M_{20} & M_{25} & M_{21} & 0 \\
\frac{\partial}{\partial r} & \frac{\partial \bar{u}_r}{\partial z} & M_2 & \frac{2m}{Rer^2} & M_{26} & M_{20}+M_{26} & M_{19} & M_{22}+M_{26} & 0 & M_{21} \\
-\frac{m}{r} & 0 & \frac{2m}{Rer^2} & M_3 & M_{27} & M_{27} & 0 & M_{23}+M_{27} & M_{19} & M_{24} \\
0 & M_5 & \frac{\partial \bar{A}_{zz}}{\partial r} & 0 & M_4+M_{28} & M_{28} & -2\frac{\partial \bar{u}_z}{\partial r} & M_{28} & 0 & 0 \\
0 & \frac{\partial \bar{A}_{rr}}{\partial z} & M_7 & 0 & M_{29} & M_6+M_{29} & -2\frac{\partial \bar{u}_r}{\partial z} & M_{29} & 0 & 0 \\
0 & M_{10} & M_9 & 0 & -\frac{\partial \bar{u}_r}{\partial z}+M_{30} & -\frac{\partial \bar{u}_z}{\partial r}+M_{30} & M_8 & M_{30} & 0 & 0 \\
0 & \frac{\partial \bar{A}_{\phi\phi}}{\partial z} & M_{12} & M_{13} & M_{31} & M_{31} & 0 & M_{11}+M_{31} & 0 & 0 \\
0 & M_{17} & 0 & M_{15} & 0 & 0 & 0 & 0 & M_{14} & -\frac{\partial \bar{u}_z}{\partial r} \\
0 & 0 & M_{17} & M_{18} & 0 & 0 & 0 & 0 & -\frac{\partial \bar{u}_r}{\partial z} & M_{16}
\end{bmatrix}. \tag{4.16}$$

The elements $M_n\,(n = 1, 31)$ in matrix $\boldsymbol{A}_d$ are shown below:

$$M_1 = \bar{u}_z\frac{\partial}{\partial z} + \bar{u}_r\frac{\partial}{\partial r} - \frac{1}{Re}\left[\frac{\partial^2}{\partial z^2} + \frac{\partial^2}{\partial r^2} + \frac{1}{r}\frac{\partial}{\partial r} - \frac{m^2}{r^2}\right] + \frac{\partial \bar{u}_z}{\partial z},$$

$$M_2 = \bar{u}_r\frac{\partial}{\partial r} + \bar{u}_z\frac{\partial}{\partial z} - \frac{1}{Re}\left[\frac{\partial^2}{\partial z^2} + \frac{\partial^2}{\partial r^2} + \frac{1}{r}\frac{\partial}{\partial r} - \frac{m^2+1}{r^2}\right] + \frac{\partial \bar{u}_r}{\partial r},$$

$$M_3 = \bar{u}_r\frac{\partial}{\partial r} + \bar{u}_z\frac{\partial}{\partial z} - \frac{1}{Re}\left[\frac{\partial^2}{\partial z^2} + \frac{\partial^2}{\partial r^2} + \frac{1}{r}\frac{\partial}{\partial r} - \frac{m^2+1}{r^2}\right] + \frac{\bar{u}_r}{r},$$

$$M_4 = \bar{u}_r\frac{\partial}{\partial r} + \bar{u}_z\frac{\partial}{\partial z} - 2\frac{\partial \bar{u}_z}{\partial z} + \frac{f(\bar{R})}{De}, \quad M_5 = \frac{\partial \bar{A}_{zz}}{\partial z} - 2\left(\bar{A}_{zr}\frac{\partial}{\partial r} + \bar{A}_{zz}\frac{\partial}{\partial z}\right) - 2\frac{\partial}{\partial z},$$

$$M_6 = \bar{u}_r\frac{\partial}{\partial r} + \bar{u}_z\frac{\partial}{\partial z} - 2\frac{\partial \bar{u}_r}{\partial r} + \frac{f(\bar{R})}{De}, \quad M_7 = \frac{\partial \bar{A}_{rr}}{\partial r} - 2\left(\bar{A}_{rr}\frac{\partial}{\partial r} + \bar{A}_{rz}\frac{\partial}{\partial z}\right) - 2\frac{\partial}{\partial r},$$

$$M_8 = \bar{u}_r\frac{\partial}{\partial r} + \bar{u}_z\frac{\partial}{\partial z} - \frac{\partial \bar{u}_r}{\partial r} - \frac{\partial \bar{u}_z}{\partial z} + \frac{f(\bar{R})}{De}, \quad M_9 = \frac{\bar{A}_{zr}}{\partial r} - \left(\bar{A}_{zr}\frac{\partial}{\partial r} + \bar{A}_{zz}\frac{\partial}{\partial z}\right) - \frac{\partial}{\partial z},$$

$$M_{10} = \frac{\bar{A}_{zr}}{\partial z} - \left(\bar{A}_{rz}\frac{\partial}{\partial z} + \bar{A}_{rr}\frac{\partial}{\partial r}\right) - \frac{\partial}{\partial r}, \quad M_{11} = \bar{u}_r\frac{\partial}{\partial r} + \bar{u}_z\frac{\partial}{\partial z} - 2\frac{\bar{u}_r}{r} + \frac{f(\bar{R})}{De},$$

$$M_{12} = \frac{\partial \bar{A}_{\phi\phi}}{\partial r} - 2\frac{\bar{A}_{\phi\phi}}{r} - \frac{2}{r}, \quad M_{13} = -\left(\frac{2\bar{A}_{\phi\phi}}{r} + \frac{2}{r}\right)m,$$

$$M_{14} = \bar{u}_r\frac{\partial}{\partial r} + \bar{u}_z\frac{\partial}{\partial z} - \frac{\bar{u}_r}{r} + \frac{f(\bar{R})}{De} - \frac{\partial \bar{u}_z}{\partial z}, \quad M_{15} = \frac{\bar{A}_{zr}}{r} - \left(\bar{A}_{zr}\frac{\partial}{\partial r} + \bar{A}_{zz}\frac{\partial}{\partial z}\right) - \frac{\partial}{\partial z},$$

$$M_{16} = \bar{u}_r\frac{\partial}{\partial r} + \bar{u}_z\frac{\partial}{\partial z} - \frac{\bar{u}_r}{r} + \frac{f(\bar{R})}{De} - \frac{\partial \bar{u}_r}{\partial r}, \quad M_{17} = -\left(\frac{\bar{A}_{\phi\phi}}{r} + \frac{1}{r}\right)m,$$

$$M_{18} = \frac{\bar{A}_{rr}}{r} - \left(\bar{A}_{rr}\frac{\partial}{\partial r} + \bar{A}_{rz}\frac{\partial}{\partial z}\right) - \left(\frac{\partial}{\partial r} - \frac{1}{r}\right), \quad M_{19} = -\frac{cf(\bar{R})}{ReDe}\frac{\partial}{\partial z},$$

$$M_{20} = -\frac{cf(\bar{R})}{ReDe}\left(\frac{\partial}{\partial r} + \frac{1}{r}\right), \quad M_{21} = -\frac{cmf(\bar{R})}{ReDe\ r},$$

$$M_{22} = \frac{cf(\bar{R})}{ReDe\ r}, \quad M_{23} = \frac{cmf(\bar{R})}{ReDe\ r}, \quad M_{24} = -\frac{cf(\bar{R})}{ReDe}\left(\frac{\partial}{\partial r} + \frac{2}{r}\right),$$

$$M_{25} = -\frac{c}{ReDe}[\nabla \cdot \bar{\boldsymbol{A}}]_z, \quad M_{26} = -\frac{c}{ReDe}[\nabla \cdot \bar{\boldsymbol{A}}]_r, \quad M_{27} = -\frac{c}{ReDe}[\nabla \cdot \bar{\boldsymbol{A}}]_\phi,$$

$$M_{28} = \frac{\bar{A}_{zz}f(\bar{R})^2}{DeL^2}, \quad M_{29} = \frac{\bar{A}_{rr}f(\bar{R})^2}{DeL^2}, \quad M_{30} = \frac{\bar{A}_{zr}f(\bar{R})^2}{DeL^2}, \quad M_{31} = \frac{\bar{A}_{\phi\phi}f(\bar{R})^2}{DeL^2}.$$

The matrix $\boldsymbol{B}_d$ has the simple form

$$\boldsymbol{B}_d = \mathrm{diag}(0, 1, 1, 1, 1, 1, 1, 1, 1, 1).$$

4.2. *Boundary conditions*

The boundary conditions for three-dimensional perturbation equations are as follows:

(*a*) Along the outer boundary. Everywhere along the entire outer boundary

$$\tilde{u}_z = \tilde{u}_r = \tilde{u}_\phi = \frac{\partial \tilde{P}}{\partial n} = 0$$

are prescribed. Based on physical intuition, it was expected (and verified upon observing the solution) that the relevant eigenfunctions are non-zero only in the vicinity of the interface and the cusp and reduce to zero very rapidly away from the interface. Thus the proposed boundary conditions, which are simple to implement, are sufficient physically. Also,

$$\begin{cases} \tilde{\boldsymbol{A}} = 0 & \text{along upstream boundary,} \\ \frac{\partial \tilde{\boldsymbol{A}}}{\partial n} = 0 & \text{along the bubble surface and sidewall.} \end{cases}$$

(*b*) Along the axis of symmetry. The boundedness and smoothness conditions are required for all physical quantities on the singular axis of geometry. Hence,

$$\lim_{r\to 0}\frac{\partial \boldsymbol{u}'}{\partial \phi} = 0, \qquad \lim_{r\to 0}\frac{\partial P'}{\partial \phi} = 0$$

given by Batchelor & Gill (1962) are applied on the centreline. Representing $\boldsymbol{u}'$, P' by (4.6), the boundary condition can be derived as follows (refer to Khorrami, Malik & Ash 1989 for details):

$$\begin{cases} \dfrac{\partial \tilde{u}_z}{\partial r} = \tilde{u}_r = \tilde{u}_\phi = \dfrac{\partial \tilde{P}}{\partial r} = 0 & \text{for } m = 0\ , \\ \tilde{u}_z = \tilde{P} = \tilde{u}_r + \tilde{u}_\phi = 2\frac{\partial \tilde{u}_r}{\partial r} + m\frac{\partial \tilde{u}_\phi}{\partial r} = 0 & \text{for } m = 1, \\ \tilde{u}_z = \tilde{u}_r = \tilde{u}_\phi = \tilde{P} = 0 & \text{for } m > 1. \end{cases} \tag{4.17}$$

For the $m = 1$ case, the relations are deduced by also enforcing the continuity equation on the symmetry axis:

$$\lim_{r\to 0}\nabla \cdot \boldsymbol{u}' = 0.$$

For polymer stretch tensor perturbations,

$$\begin{cases} \dfrac{\partial \tilde{\boldsymbol{A}}}{\partial r} = 0 & \text{for } m = 0, \\ \tilde{\boldsymbol{A}} = 0 & \text{for } m > 0. \end{cases}$$

(*c*) Along the free surface. the boundary conditions for the perturbations are obtained by subtracting basic state parts from the linearized boundary conditions for the flow variables. For the pressure (P) and velocity components (u_z, u_r, u_ϕ), the dynamic conditions of the free surface consist of (3.6), (3.7) and

$$\frac{1}{r}\frac{\partial u_n}{\partial \phi} + \frac{\partial u_\phi}{\partial n} - \frac{u_\phi n_r}{r} + c\sigma^p_{n\phi} = 0, \tag{4.18}$$

and the continuity equation gives

$$\frac{\partial u_n}{\partial n} + \frac{\partial u_s}{\partial s} + \frac{u_r}{r} + \frac{1}{r}\frac{\partial u_\phi}{\partial \phi} = 0. \tag{4.19}$$

The unit normal and tangential vectors on the bubble surface ($\boldsymbol{n}, \boldsymbol{s}$) are decomposed into the base-state part ($\bar{\boldsymbol{n}}, \bar{\boldsymbol{s}}$) and small disturbances ($\boldsymbol{n}', \boldsymbol{s}'$). The base-state parts $\bar{\boldsymbol{n}}, \bar{\boldsymbol{s}}$ are given as

$$\bar{n}_r = \bar{s}_z = \frac{\dfrac{\partial \bar{z}}{\partial \bar{s}}}{\left[\left(\dfrac{\partial \bar{z}}{\partial \bar{s}}\right)^2 + \left(\dfrac{\partial \bar{r}}{\partial \bar{s}}\right)^2\right]^{\frac{1}{2}}},$$

$$-\bar{n}_z = \bar{s}_r = \frac{\dfrac{\partial \bar{r}}{\partial \bar{s}}}{\left[\left(\dfrac{\partial \bar{z}}{\partial \bar{s}}\right)^2 + \left(\dfrac{\partial \bar{r}}{\partial \bar{s}}\right)^2\right]^{\frac{1}{2}}},$$

$$\bar{n}_\phi = 0.$$

Caused by the normal disturbance of the surface (H'_n), the 'small' vectors $\boldsymbol{n}'$, $\boldsymbol{s}'$ are derived as

$$n'_z = -s'_r = -\bar{n}_r\left(1 - \bar{n}_z^2\right)\frac{\dfrac{\partial r'}{\partial \bar{s}}\dfrac{\partial \bar{z}}{\partial \bar{s}} - \dfrac{\partial \bar{r}}{\partial \bar{s}}\dfrac{\partial z'}{\partial \bar{s}}}{\left(\dfrac{\partial \bar{z}}{\partial \bar{s}}\right)^2},$$

$$n'_r = s'_z = \bar{n}_z\bar{n}_r^2\frac{\dfrac{\partial r'}{\partial \bar{s}}\dfrac{\partial \bar{z}}{\partial \bar{s}} - \dfrac{\partial \bar{r}}{\partial \bar{s}}\dfrac{\partial z'}{\partial \bar{s}}}{\left(\dfrac{\partial \bar{z}}{\partial \bar{s}}\right)^2},$$

$$n'_\phi = -\frac{\bar{n}_r}{\bar{r}}\left(\frac{\partial r'}{\partial \phi} + \frac{\bar{n}_z}{\bar{n}_r}\frac{\partial z'}{\partial \phi}\right),$$

where

$$z' = H'_n\bar{n}_z, \quad r' = H'_n\bar{n}_r$$

are the projections of the normal displacement perturbation H_n' in the axial and radial directions, respectively. The pressure and velocity perturbations along the bubble surface are functions of surface coordinate s and normal displacement H_n and are linearized as follows:

$$P'(s, H_n) = P'(\bar{s}, 0) + \frac{\partial \bar{P}}{\partial \bar{n}} H_n' + H.O.T.,$$

$$u_z'(s, H_n) = u_z'(\bar{s}, 0) + \frac{\partial \bar{u}_z}{\partial \bar{n}} H_n' + H.O.T.,$$

$$u_r'(s, H_n) = u_r'(\bar{s}, 0) + \frac{\partial \bar{u}_r}{\partial \bar{n}} H_n' + H.O.T.,$$

where $H.O.T.$ denotes higher order terms, which are neglected.

Utilizing the above expressions to subtract the base-state part from (3.6), (3.7), (4.18) and (4.19), the perturbed normal stress balance condition, applied on the basic state shape, is derived as

$$P' + \frac{\partial \bar{P}}{\partial \bar{n}} H_n' + \frac{z'}{Re} - \frac{2}{Re}(\bar{\boldsymbol{n}} \cdot \nabla(\boldsymbol{u}' \cdot \bar{\boldsymbol{n}}) + \bar{\boldsymbol{n}} \cdot \nabla(\bar{\boldsymbol{u}} \cdot \boldsymbol{n}') + \boldsymbol{n}' \cdot \nabla(\bar{\boldsymbol{u}} \cdot \bar{\boldsymbol{n}})) - \frac{c}{Re}(\bar{\boldsymbol{n}} \cdot \sigma^{p\prime} \cdot \bar{\boldsymbol{n}} + 2\bar{\boldsymbol{n}} \cdot \bar{\sigma}^{p} \cdot \mathbf{n}') + \frac{\nabla \cdot \mathbf{n}'}{Re\ Ca} = 0. \tag{4.20}$$

Similarly, the two tangential stress balance conditions are given as

$$(\bar{\boldsymbol{s}} \cdot \nabla(\boldsymbol{u}' \cdot \bar{\boldsymbol{n}}) + \bar{\boldsymbol{s}} \cdot \nabla(\bar{\boldsymbol{u}} \cdot \boldsymbol{n}') + \boldsymbol{s}' \cdot \nabla(\bar{\boldsymbol{u}} \cdot \bar{\boldsymbol{n}})) + (\bar{\boldsymbol{n}} \cdot \nabla(\bar{\boldsymbol{u}} \cdot \boldsymbol{s}') + \bar{\boldsymbol{n}} \cdot \nabla(\boldsymbol{u}' \cdot \bar{\boldsymbol{s}}) + \boldsymbol{n}' \cdot \nabla(\bar{\boldsymbol{u}} \cdot \bar{\boldsymbol{s}})) + c(\bar{\boldsymbol{n}} \cdot \sigma^{p\prime} \cdot \bar{\boldsymbol{s}} + \mathbf{n}' \cdot \bar{\sigma}^{p} \cdot \bar{\mathbf{s}} + \bar{\mathbf{n}} \cdot \bar{\sigma}^{p} \cdot \mathbf{s}') = 0 \tag{4.21}$$

and

$$\left(\frac{1}{\bar{r}} \frac{\partial}{\partial \phi}(\bar{\boldsymbol{u}} \cdot \boldsymbol{n}' + \boldsymbol{u}' \cdot \bar{\boldsymbol{n}}) + \frac{\partial u_\phi'}{\partial \bar{n}}\right) - \frac{u_\phi' \bar{n}_r}{\bar{r}} + c(\sigma_{z\phi}^{p\prime} \bar{n}_z + \sigma_{r\phi}^{p\prime} \bar{n}_r) = 0. \tag{4.22}$$

respectively. The continuity equation along the free boundary is perturbed as

$$(\bar{\boldsymbol{n}} \cdot \nabla(\boldsymbol{u}' \cdot \bar{\boldsymbol{n}}) + \bar{\boldsymbol{n}} \cdot \nabla(\bar{\boldsymbol{u}} \cdot \boldsymbol{n}') + \boldsymbol{n}' \cdot \nabla(\bar{\boldsymbol{u}} \cdot \bar{\boldsymbol{n}})) + (\bar{\boldsymbol{s}} \cdot \nabla(\bar{\boldsymbol{u}} \cdot \boldsymbol{s}') + \bar{\boldsymbol{s}} \cdot \nabla(\boldsymbol{u}' \cdot \bar{\boldsymbol{s}}) + \boldsymbol{s}' \cdot \nabla(\bar{\boldsymbol{u}} \cdot \bar{\boldsymbol{s}})) + \frac{1}{\bar{r}} \frac{\partial u_\phi'}{\partial \phi} + \frac{u_r'}{\bar{r}} - \frac{\bar{u}_r}{\bar{r}^2} r' = 0. \tag{4.23}$$

The perturbed kinematic condition describes the effect of the small displacement on the shape of the free surface:

$$\frac{\partial H_n'}{\partial t} + \bar{\boldsymbol{u}} \cdot \nabla H_n' = \boldsymbol{u}' \cdot \bar{\boldsymbol{n}}. \tag{4.24}$$

The boundary condition for polymer stretch tensor perturbations, $\boldsymbol{A}'$, is similar to its base-state counterpart:

$$\frac{\partial \boldsymbol{A}'}{\partial \bar{n}} = 0. \tag{4.25}$$

By inserting (4.6) for $\boldsymbol{Q}'$, the free-surface conditions (4.20)–(4.25) can be cast in the matrix equation form of

$$\boldsymbol{A}_b \tilde{\boldsymbol{X}}_b = -\omega \boldsymbol{B}_b \tilde{\boldsymbol{X}}_b, \tag{4.26}$$

where

$$\tilde{\mathbf{X}}_b = \begin{bmatrix} \tilde{P} \\ \tilde{\boldsymbol{u}} \\ \tilde{\boldsymbol{A}} \\ \tilde{H}_n \end{bmatrix} (z_b, r_b) \tag{4.27}$$

denotes the eigenfunction restricted to the free-boundary points. In the matrix $\boldsymbol{B}_b$, only the diagonal element corresponding to normal displacement $\tilde{H}_n$ is unity, all other elements are zero.

Other boundary conditions for perturbations can be cast in the general matrix form of (4.26) as well. The complete matrix equation for this generalized eigenvalue problem is formed by combining (4.12) and (4.26):

$$\begin{bmatrix} \boldsymbol{A}_d & 0 \\ 0 & \boldsymbol{A}_b \end{bmatrix} \begin{bmatrix} \tilde{\boldsymbol{X}}_d \\ \tilde{\boldsymbol{X}}_b \end{bmatrix} = -\omega \begin{bmatrix} \boldsymbol{B}_d & 0 \\ 0 & \boldsymbol{B}_b \end{bmatrix} \begin{bmatrix} \tilde{\boldsymbol{X}}_d \\ \tilde{\boldsymbol{X}}_b \end{bmatrix}. \tag{4.28}$$

4.3. *Computational method*

The generalized partial-differential eigenvalue problem (4.28) governs the dispersion relation of the temporal exponent, ω, and azimuthal wavenumbers, m, of the small disturbances for a specific combination of capillary number, Ca, Reynolds number, Re, and Deborah number, De. All terms are discretized over the computational domain, using central-differencing scheme. The numerical eigenvalue problem is then solved iteratively by the software package ARPACK (Lehoucq, Sorensen & Yang 1997) for the leading eigenvalue (ω) representing the most unstable mode. ARPACK is an eigenvalue solver based on the Arnoldi method (Sorensen 1992) which is most appropriate for large-scale matrix computations. In solving the eigenvalue problem, much care is needed to discern the physical eigenvalues from the large population of the numerical eigenvalues. A criterion to identify the physical eigenvalue is to check whether the corresponding eigenfunctions are physically reasonable. The spurious numerical eigenvalues are accompanied by non-physical eigenfunctions. Furthermore and more quantitatively, the physical dimensions of the meshed domain were changed for the same case to ensure the obtained physical eigenvalues are mesh-independent and unaffected by the above change.

4.4. *Energy budget equation*

In order to understand the mechanism responsible for cusp instability, the equation governing the kinetic energy of small disturbances is investigated term by term. This energy equation is derived from the momentum equation (4.8) as

$$\underbrace{\frac{D}{Dt}\int_v \frac{u_i' u_i'}{2}\,\mathrm{d}V}_{K.E.} = \underbrace{\int_v -u_i' u_j' \frac{\partial \bar{U}_i}{\partial x_j}\,\mathrm{d}V}_{E_s} \underbrace{- \int_v \frac{\partial (P' u_i')}{\partial x_i}\,\mathrm{d}V}_{E_p} + \underbrace{\frac{1}{Re}\int_v \frac{\partial^2}{\partial x_j^2}\left(\frac{u_i' u_i'}{2}\right)\mathrm{d}V}_{E_v}$$
$$\underbrace{- \frac{1}{Re}\int_v \left(\frac{\partial u_i'}{\partial x_j}\right)^2 \mathrm{d}V}_{E_d} + \underbrace{\frac{c}{Re}\int_v u_i' \frac{\partial \sigma_{ij}^{p'}}{\partial x_j}\,\mathrm{d}V}_{E_f}. \tag{4.29}$$

The identifiers associated with the underbraces in (4.29) are described below:
$K.E.$: total kinetic energy of small disturbances corresponding to an eigenmode over a control volume;

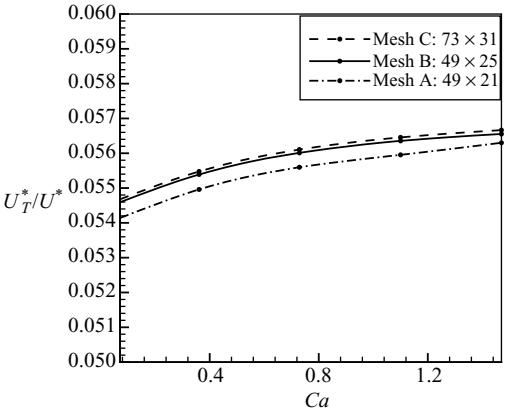

FIGURE 2. Normalized terminal velocity (U_T^*/U^*) versus capillary number (Ca_T) for different mesh resolutions: a gas bubble rising in an FENE-CR fluid with $L = 3$.

E_s: production or destruction of energy through the interaction of base-state velocity gradient and Reynolds stresses;
E_p: energy change through the pressure gradient;
E_v: energy change due to viscous effects;
E_d: energy change due to viscous dissipation;
E_f: energy change through the polymer stress gradient.
Among the above terms, the following results (in § 6.3) indicate E_p is the largest contribution to $K.E.$ increase. By applying the divergence theorem to E_p over the whole domain and in view of the vanishing of velocity disturbances on the outer boundary, E_p can be expressed as the net energy flux across the bubble surface caused by the pressure disturbance:

$$-\int_v \frac{\partial(P'u_i')}{\partial x_i}\,\mathrm{d}V = -\oint_S P'\boldsymbol{u}'\cdot\,\mathrm{d}\boldsymbol{s}. \tag{4.30}$$

Then applying the normal stress balance condition (4.20) to replace P', the energy change over the entire volume due to E_p becomes

$$-\int_v \frac{\partial(P'u_i')}{\partial x_i}\,\mathrm{d}V = \oint_S \left\{ \frac{\partial \bar{P}}{\partial \bar{n}} H_n' + \frac{z'}{Re} - \frac{2}{Re}[\bar{\boldsymbol{n}}\cdot\nabla(\boldsymbol{u}'\cdot\bar{\boldsymbol{n}}) + \bar{\boldsymbol{n}}\cdot\nabla(\bar{\boldsymbol{u}}\cdot\boldsymbol{n}') + \boldsymbol{n}'\cdot\nabla(\bar{\boldsymbol{u}}\cdot\bar{\boldsymbol{n}})] \right.$$
$$\left. - \frac{c}{Re}(\bar{\boldsymbol{n}}\cdot\sigma^{p'}\cdot\bar{\boldsymbol{n}} + 2\bar{\boldsymbol{n}}\cdot\bar{\sigma}^{p}\cdot\boldsymbol{n}') + \frac{\nabla\cdot n'}{Re\ Ca} \right\} \boldsymbol{u}'\cdot(-\bar{\boldsymbol{n}})\,\mathrm{d}S. \tag{4.31}$$

In § 6.3, we will use (4.31) in energy analysis of bubble cusp instability.

5. Base flow results

The cylindrical tube is modelled as a computational domain that extends $10D$ in the axial direction and $5D$ in radial direction. The initially spherical bubble of diameter D is at the origin. A boundary-fitted mesh is generated at each time step to match the deforming bubble surface. A complete description of adaptive mesh generation for this work is included in the paper by You *et al.* (2008). A mesh-dependence study is performed for three levels of refinement as shown in figure 2. The steady-state results based on the three mesh refinements indicate that the terminal rise speed of the bubble for a range of capillary numbers converges on the mesh refinement with

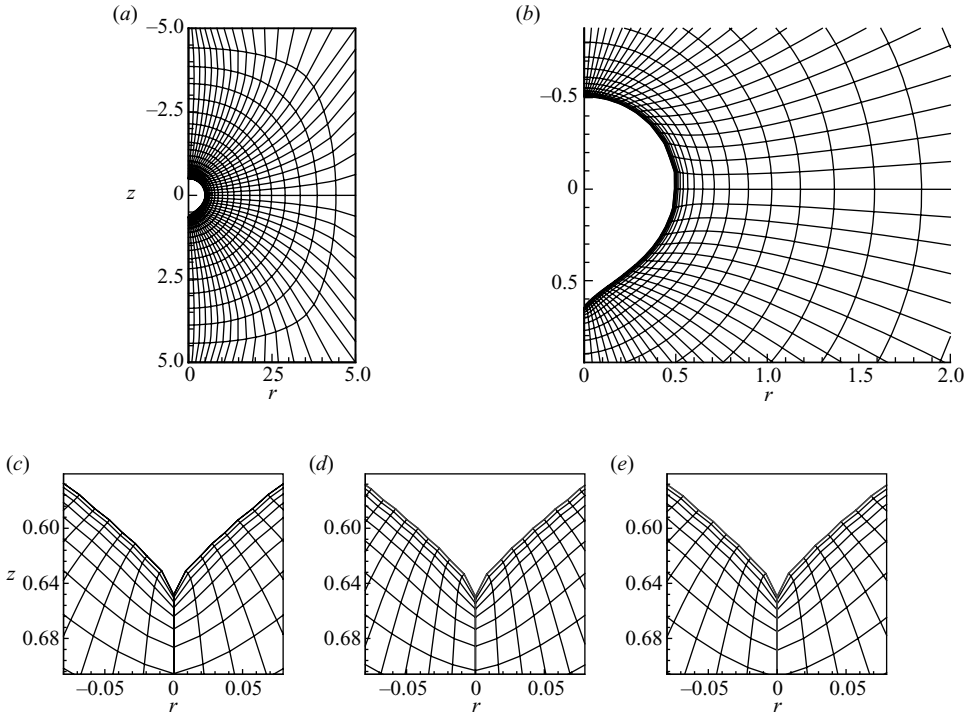

FIGURE 3. Overall and close-up views of the boundary-fitted mesh around an axisymmetric cusped bubble rising in an FENE-CR fluid with $L = 3$, $De_T = 0.452$, $Re_T = 0.435$, $Ca_T = 1.469$, $c = 0.3$: (*a*) 49 × 25 points; (*b*) 49 × 25 points; (*c*) 49 × 25 points; (*d*) 73 × 31 points; (*e*) 49 × 21 points.

49 (meridional) × 25 (radial) points. The overall and close-up meshes around the Z–r cross-section of an axisymmetric cusped bubble rising in an FENE-CR fluid are shown in figure 3. As figure 3(*b*) shows, the meridional distribution of points on the bubble surface cluster around the two poles in order to effectively resolve the large curvature changes there. Figure 3(*c–e*) shows a comparison of three different mesh resolutions around the tip for the same physical conditions. The smallest cell size (in the radial direction) adjacent to the bubble surface is uniformly specified as $0.002D$ for all three meshes presented. An effectively identical curvature around the tip is achieved for all three levels of mesh refinement. As per the axisymmetric curvature formula (3.8), the corresponding three-dimensional curvatures of the first off-axis cell surface adjacent to the tip point are 187, 187 and 186 based on 49 × 25, 73 × 31 and 49 × 21 mesh configurations, respectively (figure 3*c–e*).

Results are computed for the physical conditions specified as $Re_T = 0.435, Ca_T = 1.469$, $De_T = 0.452$, $c = 0.3$. In the FENE-CR model equations, the maximal extension of polymer chains is specified as $L = 3.0$. This set of parameters was one that supports a knife-edge cusp. An extensive search of the parameter space was conducted before this set, and several others like it were identified. This is consistent with the rarity of the knife-edge cusp in experiments. Figure 4(*a*) records the bubble-rising velocity with respect to time. It shows a steep increase in velocity during the initial time and quick convergence to the terminal velocity. The transient shapes are shown in figure 4(*b*). The bubble deforms from a sphere to a prolate shape with a round tip and finally develops a sharp axisymmetric trailing edge in about 4.5

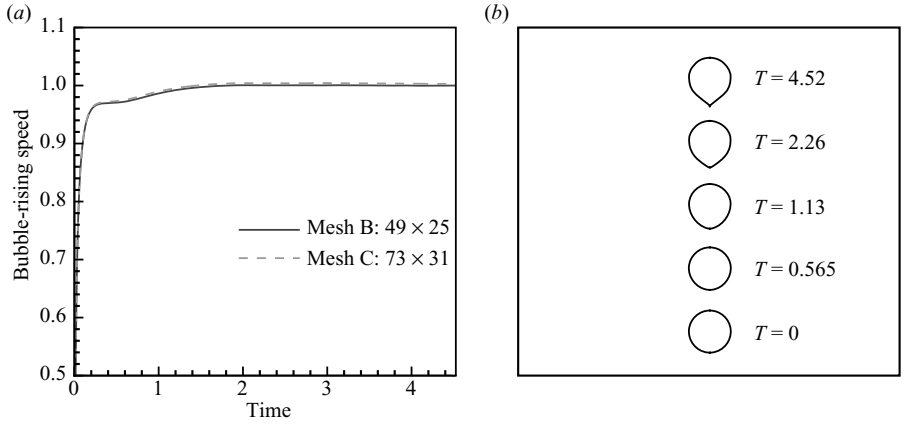

FIGURE 4. Transient states of a gas bubble rising in an FENE-CR fluid with $L = 3$, $Re_T = 0.435$, $Ca_T = 1.469$, $De_T = 0.452$, $c = 0.3$: (a) time history of bubble-rising velocity (dimensionless); (b) time history of deforming shapes.

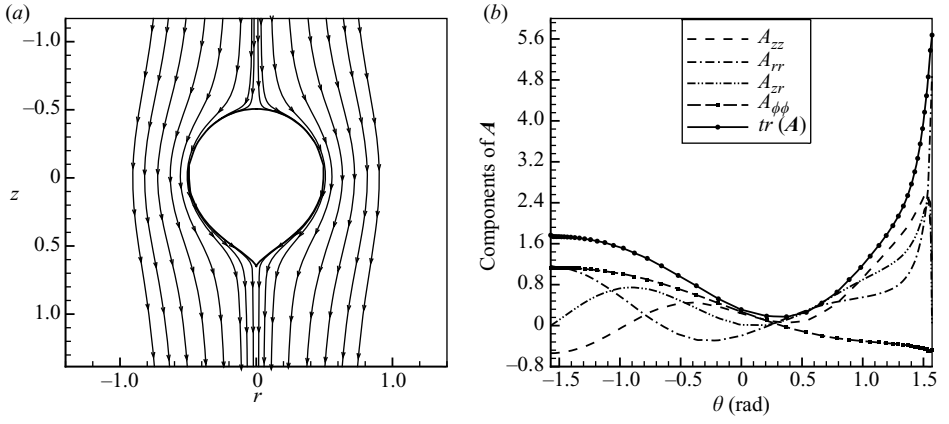

FIGURE 5. Converged base-state solution of a gas bubble in an FENE-CR fluid with $L = 3$, $Re_T = 0.435$, $Ca_T = 1.469$, $De_T = 0.452$, $c = 0.3$, $T = 4.52$: (a) streamlines around a gas bubble; (b) distribution of $\boldsymbol{A}$ along the bubble surface; θ increases from top to bottom.

time units. Here, a time unit denotes the time required for the bubble to move one diameter at the terminal speed of U_T^*. At $T = 4.52$, a steady-state shape is reached, as streamlines strictly conform to the bubble surface (figure 5a). The strongest stretching is around the cusped tip as indicated by $tr(\boldsymbol{A})$ (figure 5b). The distribution of the components of the polymer stretch tensor $\boldsymbol{A}$ on the bubble surface is also plotted in the figure. A peak value for A_{rr} at the tip indicates a strong radial stretching experienced by the cusped tip.

6. Stability analysis results

In the preceding section, a base-state solution is presented. An axisymmetric cusp is developed at the trailing edge. But the question remains as to whether this axisymmetric cusp is actually observable in the presence of disturbances. To answer this question, the linear stability analysis is carried out by introducing three-dimensional small disturbances $\boldsymbol{Q}'$ in the form of (4.6) to perturb the base-state

Mesh A (49 × 21) $N = 11008$	Mesh B (49 × 25) $N = 13008$	Mesh C (73 × 31) $N = 23712$
+0.143036*	+0.143843*	+0.144751*
−0.157106	−1.627342	−0.156029
−0.178140 ± 0.0529013i	−0.172514 ± 0.0552610i	−0.172019 ± 0.0560471i
−0.188236 ± 0.0816902i	−0.185163 ± 0.0837109i	−0.185150

TABLE 1. The five leading eigenvalues (ω) for different meshes at $m = 2$: a gas bubble rising in an FENE-CR fluid with $L = 3$, $D_t/D = 10$, $Re_T = 0.435$, $Ca_T = 1.469$, $De_T = 0.452$, $c = 0.3$.

solution $\bar{\boldsymbol{Q}}$. For a specified azimuthal wavenumber m, the generalized eigenvalue problem (4.28) is solved for the leading eigenvalue (ω) which indicates the growth rate of the most unstable eigenmode. For the critical eigenmode, an arbitrary but small amplitude of the corresponding eigenfunction is combined with the base-state solution to reconstruct an unstable three-dimensional flow field around the cusped bubble. An investigation of the energy budget of the disturbances is performed to determine the production and dissipation terms affecting the growth of this flow instability.

6.1. *Validation study*

It is important to pinpoint the leading physical eigenvalue among a number of numerical eigenvalues in the eigenvalue problem. A criterion to identify the physical one from a large population of numerical eigenvalues is to check whether the corresponding eigenvectors are physically understandable. The spurious eigenvalues are accompanied by non-physical, randomly oscillating eigenvectors. To ensure the accuracy of the numerical results, we employed three meshes of different resolutions to study the flow for $Re_T = 0.435$, $Ca_T = 1.469$, $De_T = 0.452$, $c = 0.3$. With each of these three meshes and corresponding base flow fields, the generalized eigenvalue problem (4.28) was formulated with a matrix of size N × N. The eigenvalues that had the smallest real values at the azimuthal wavenumber $m = 2$ were taken as the first five eigenvalues. The comparison of computed eigenvalues for three different meshes are made in table 1. The only positive ω (with the superscript*) is identified as the leading eigenvalue with very small variations among these three meshes. This positive real eigenvalue represents the growth rate of the unstable eigenmode at $m = 2$. In the following sections, the intermediate mesh with 49×25 points is used to present results.

6.2. *The least stable eigenmode*

The superposition of a base-state shape and a three-dimensional shape disturbance will give rise to a deformed shape as a function of azimuthal wavenumber. A sketch is drawn in figure 6 to illustrate schematic bubble shapes with surface perturbations with various wavenumbers. The perturbation with $m = 2$ is the only one that can turn an axisymmetric bubble into a 'knifelike' shape.

The least stable eigenvalues, ω, corresponding to different azimuthal wavenumbers, m, are listed in table 2. A study of this table shows that, except for $m = 0$, which represents the axisymmetric perturbation, all eigenvalues corresponding to $m > 0$ have no imaginary part ($\mathrm{Im}(\omega) = 0$). This means that the development of three-dimensionality is not a Hopf-type bifurcation but an exchange of stabilities. The only positive ω, which represents the growth rate of an unstable mode, occurs for $m = 2$. The small disturbances for all other modes decay. As explained in the sketch

m	Leading eigenvalue (ω)
0	$-1.35848 \times 10^{-1} \pm 0.0110893$i
1	-1.82535×10^{-2}
2	$+1.43843 \times 10^{-1}$
3	-3.66268×10^{-2}
4	-1.64677×10^{-1}
5	-2.27981×10^{-1}
6	-2.30643×10^{-1}
7	-2.33831×10^{-1}
8	-2.37438×10^{-1}

TABLE 2. Leading eigenvalues (ω) versus azimuthal wavenumber (m): a gas bubble rising in an FENE-CR fluid with $L=3$, $D_t/D=10$, $Re_T=0.435$, $Ca_T=1.469$, $De_T=0.452$, $c=0.3$.

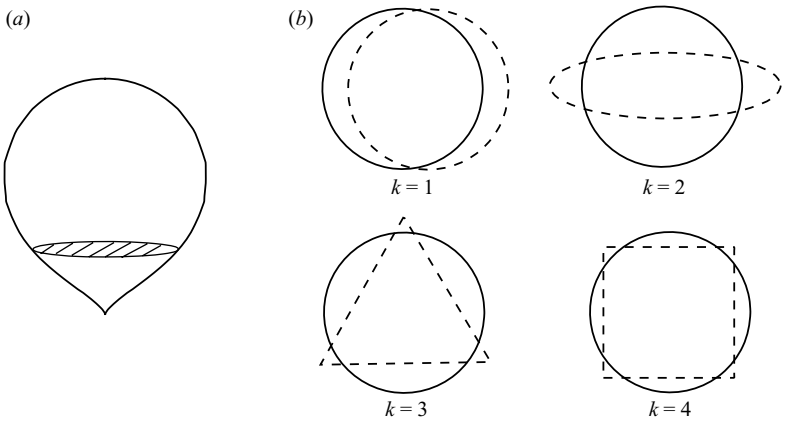

FIGURE 6. (a) A sketch of a cusped bubble. (b) Top views of the cross-sections at different azimuthal wave numbers (m): the solid line denotes an unperturbed cross-section; the dashed line denotes a perturbed cross-section at the corresponding m.

(figure 6), the eigenmode with $m=2$ has the effect of flattening an axisymmetric bubble. The value $\omega=0.143843$ means that it requires 6.95 unit computational time, which is equivalent to 0.392 unit time (as defined above, 1 unit time denotes the time required for the bubble to move the distance of $1D$ at the speed U_T^*), for an e-folding of the initial disturbances. Compared with 4.52 unit time for a complete base-state bubble deformation, 0.392 unit time represents a very short time period to form a three-dimensional cusp. As the azimuthal wavenumber, m, increases above 2, small disturbances of the corresponding eigenmode are damped at an increasing rate of $\mathrm{Re}(\omega)$. Figure 7 shows that the normal displacement eigenfunction, $\tilde{H}_n$, on the bubble surface for $m=2$ mode; $\tilde{H}_n$ is nearly zero in the front part and grows rapidly near the rear part. It then ends up at zero at the tip due to the restriction of the boundary condition (4.17). This causes a steep gradient of $\tilde{H}_n$ close to the rear tip. The $\tilde{H}_n$ eigenfunction implies a nearly unperturbed front surface and largely disturbed rear surface. The imposed boundary condition of zero perturbation on the singular axis for $m>1$ is an artefact of the perturbation approach, compared with a fully three-dimensional simulation. The latter would not have been restricted by the boundary condition; however, the cost and complexity would have been drastically higher. Furthermore, the results would have been less insightful. In figure 8, the velocity

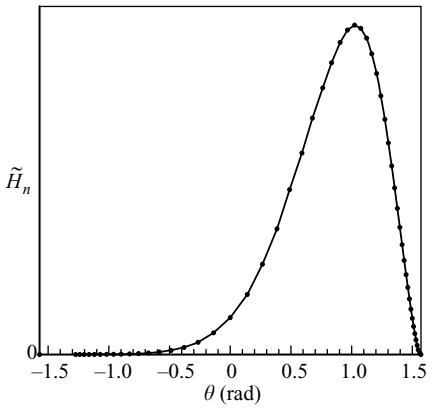

FIGURE 7. Distribution of normal displacement eigenvector ($\tilde{H}_n$) along the bubble surface for the unstable eigenmode with $m=2$; θ increases from top to tail; a gas bubble rising in an FENE-CR fluid with $L=3$, $D_t/D=10$, $Re_T=0.435$, $Ca_T=1.469$, $De_T=0.452$, $c=0.3$.

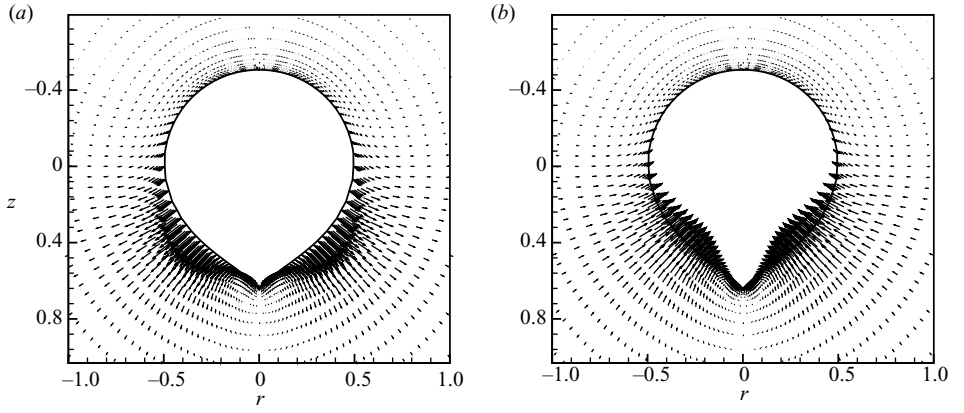

FIGURE 8. Velocity perturbation field ($\boldsymbol{u}'$) in two azimuthally perpendicular planes for the unstable eigenmode with $m=2$: a gas bubble rising in a FENE-CR fluid with $L=3$, $D_t/D=10$, $Re_T=0.435$, $Ca_T=1.469$, $De_T=0.452$, $c=0.3$. (*a*) $\boldsymbol{u}'$ in one plane; (*b*) $\boldsymbol{u}'$ in the perpendicular plane.

perturbation vectors ($\boldsymbol{u}'$) in two azimuthally perpendicular planes also exhibit their most prominent gradients very close to the rear tip for $m=2$. In one plane, the velocity perturbations intend to push the rear surface inward, while in an orthogonal plane, they try to stretch the surface out.

The three-dimensional perturbed bubble shape for the unstable mode with $m=2$ is generated by superposition of the base-state shape, and the bubble surface normal displacement disturbance H' as expressed by

$$H'(z,r,\phi)=\epsilon\tilde{H}_n(z,r)\cos(m\phi)e^{\omega t}.$$

In the above formulation, ϵ and t are two arbitrary parameters; ϵ represents an arbitrary amount of the small disturbance eigenfunction; and t denotes an arbitrary value for time. In this particular case, $\epsilon=0.2$, $t=0.1$ are specified to generate the three-dimensional shape as shown in figure 9. It clearly shows a knifelike cusped tail with a sharp trailing edge in one view and a broad edge in the perpendicular view.

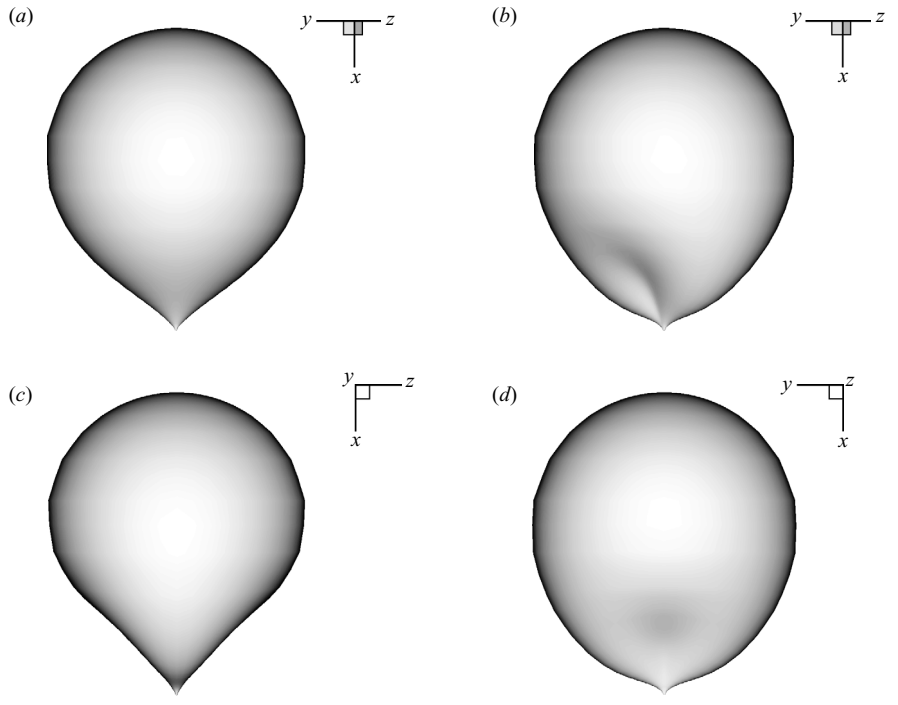

FIGURE 9. Comparison of (*a*) the axisymmetric cusp shape of base-state solution and (*b*) the knifelike cusp shape for the unstable mode with $m = 2$; (*c*) and (*d*) represent mutually perpendicular views of the knifelike cusp shape: a gas bubble rising in a FENE-CR fluid with $L = 3$, $D_t/D = 10$, $Re_T = 0.435$, $Ca_T = 1.469$, $De_T = 0.452$, $c = 0.3$. (*a*) Base-state shape; (*b*) perturbed shape; (*c*) cusp view; (*d*) broad edge view.

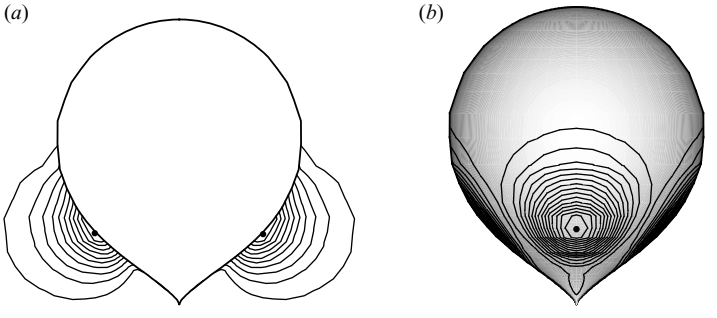

FIGURE 10. Kinetic energy increase rate for the eigenmode with $m = 2$; the maximum value is marked by the point; each contour line away from the point represents a decreasing level of kinetic energy rate: a gas bubble rising in an FENE-CR fluid with $L = 3$, $D_t/D = 10$, $Re_T = 0.435$, $Ca_T = 1.469$, $De_T = 0.452$, $c = 0.3$. (*a*) z–r plane view; (*b*) on the bubble surface.

6.3. *Energy budget analysis*

To understand the mechanism leading to the knifelike cusp instability, the energy budget equation (4.29) for the unstable eigenmode with $m = 2$ is investigated. Figure 10 presents the time rate of change of the disturbance kinetic energy ($K.E.$) in the flow field. It shows that the most energized region is located on the rear bubble surface at which the maximal surface disturbance occurs. The integration of each energy term in

E_p	7.46
E_v	1.69
E_s	−0.06
E_f	−1.71
E_d	−6.38
$\frac{D}{Dt}$ $K.E.$	1.00

TABLE 3. Energy budget for the eigenmode with $m=2$ (4.29): a gas bubble rising in an FENE-CR fluid with $L=3$, $D_t/D=10$, $Re_T=0.435$, $Ca_T=1.469$, $De_T=0.452$, $c=0.3$.

1	2.035
2	−0.185
3	−0.229
4	−0.078
5	0.066
6	0.138
7	−0.002
8	−0.745
E_p	1.00

TABLE 4. E_p decomposition for the eigenmode with $m=2$ (6.1): a gas bubble rising in an FENE-CR fluid with $L=3$, $\frac{D_t}{D}=10$, $Re_T=0.435$, $Ca_T=1.469$, $De_T=0.452$, $c=0.3$.

(4.29) over the entire domain represents its contribution to the total $K.E.$ change. Normalized by the sum of all terms, the calculations in table 3 indicate that E_d provides a major dissipation of the total $K.E.$; E_f represents a small dissipation resulting from the coupling of two small perturbation terms; E_s is a small disturbance energy destruction term that damps the disturbances slightly; E_v contributes to energy production of small disturbances; E_p is the major energy production term of $K.E.$ The role of E_v can be demonstrated via a qualitative analysis of the velocity perturbation field in figure 8: the velocity magnitude decreases in the normal direction away from the bubble surface. Since the energy contribution by E_v over the whole domain is given by

$$E_v = \frac{1}{Re}\int_v \frac{\partial^2}{\partial x_j^2}\left(\frac{u_i' u_i'}{2}\right)\mathrm{d}V = \oint_S \nabla\left(\frac{\boldsymbol{u}'\cdot\boldsymbol{u}'}{2}\right)\cdot(-\bar{\boldsymbol{n}})\,\mathrm{d}S,$$

($\bar{\boldsymbol{n}}$ points outward the surface) E_v turns out to be positive in this surface integral. For the term E_p, (4.31) provides a mechanism for energy transport from the base flow to the perturbations through the bubble surface. In order to understand the mechanism, term by term calculation of (4.31) was performed. For convenience, this equation is rearranged as

$$\begin{aligned} E_p = -\int_v \frac{\partial(P'u_i')}{\partial x_i}\,\mathrm{d}V = \oint_S \Bigg\{ &\underbrace{-\left(\frac{\partial \bar{P}}{\partial \bar{n}}H_n'\right)(\boldsymbol{u}'\cdot\bar{\boldsymbol{n}})}_{(1)} + \underbrace{\frac{z'}{Re}\boldsymbol{u}'\cdot(-\bar{\boldsymbol{n}})}_{(2)} + \underbrace{\frac{2}{Re}\bar{\boldsymbol{n}}\cdot\nabla(\boldsymbol{u}'\cdot\bar{\boldsymbol{n}})\boldsymbol{u}'\cdot(\bar{\boldsymbol{n}})}_{(3)} \\ &+ \underbrace{\frac{2}{Re}\bar{\boldsymbol{n}}\cdot\nabla(\bar{\boldsymbol{u}}\cdot\boldsymbol{n}')\boldsymbol{u}'\cdot(\bar{\boldsymbol{n}})}_{(4)} + \underbrace{\frac{2}{Re}\boldsymbol{n}'\cdot\nabla(\bar{\boldsymbol{u}}\cdot\bar{\boldsymbol{n}})\boldsymbol{u}'\cdot(\bar{\boldsymbol{n}})}_{(5)} \\ &+ \underbrace{\frac{c}{Re}\bar{\boldsymbol{n}}\cdot\sigma^{p'}\cdot\bar{\boldsymbol{n}}\boldsymbol{u}'\cdot(\bar{\boldsymbol{n}})}_{(6)} + \underbrace{\frac{c}{Re}2\bar{\boldsymbol{n}}\cdot\bar{\sigma}^{p}\cdot\boldsymbol{n}'\boldsymbol{u}'\cdot(\bar{\boldsymbol{n}})}_{(7)} + \underbrace{\frac{\nabla\cdot\boldsymbol{n}'}{Re\ Ca}\boldsymbol{u}'\cdot(-\bar{\boldsymbol{n}})}_{(8)} \Bigg\}\,\mathrm{d}S, \end{aligned} \tag{6.1}$$

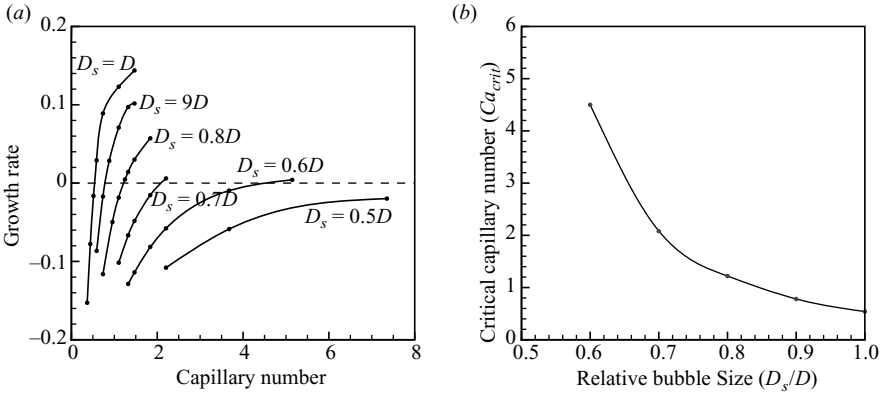

FIGURE 11. The effect of capillary number and bubble size on disturbance growth rate at $D_t/D = 10$, $Re_T = 0.435$, $De_T = 0.452$, $c = 0.3$, $m = 2$: the FENE-CR model with $L = 3$. (*a*) Growth rate (ω) versus capillary number (Ca_T) and bubble size (D_s); (*b*) critical capillary number versus bubble size.

then the surface integral of each term (1–8) over the whole bubble surface is calculated and normalized by the sum of all terms in E_p. The results are listed in table 4. It shows that term (1), which represents the triple interaction among the base-state pressure gradient ($\partial \bar{P}/\partial \bar{n}$), the normal displacement perturbation (H_n') and the normal velocity perturbation (u_n') on the freesurface, is the dominant contributor to E_p and subsequently to $K.E.$ of small disturbances. The first set of parentheses is basically the change of base pressure as a result of the motion of the surface under the perturbation; the second set of parentheses is the perturbed normal velocity. The combination denotes the p–V work done by the base pressure on the perturbed volume. Therefore, it is concluded that this term causes knifelike cusp instability to appear. To further verify the conclusion, a simple test was carried out by turning off $\partial \bar{P}/\partial \bar{n}$ in the boundary conditions for perturbed equations. The resulting leading eigenvalue, ω, became a positive value, which meant a stable eigenmode with $m = 2$ would exist if $\partial \bar{P}/\partial \bar{n} = 0$.

6.4. *Effects of bubble size and surface tension*

A parametric study was conducted to investigate the effect of bubble size and surface tension on bubble cusp formation in a viscoelastic fluid of a fixed Deborah number. In order to make the comparison, the flow conditions are kept the same for all cases, i.e. the FENE-CR model fluid with $L = 3$, $Re_T = 0.435$, $De_T = 0.452$, $c = 0.3$. The bubble size, D_s, varies from $0.5D$ to D while the tube diameter is always fixed as $D_t = 10D$. The effect of surface tension is represented by the capillary number based on U_T^* and μ for the case with $D_s = D$. At $m = 2$, the growth rate, ω, as a function of Ca_T and D_s is plotted in figure 11(*a*). It can be seen that ω increases as Ca_T increases for a given bubble size (D_s) and a fixed Deborah number (De_T). There exists a critical value of Ca_T at the intersection point of each curve with $\omega = 0$, and the knifelike cusp instability will occur when Ca_T is increased above it. This critical Ca_T increases as the bubble size decreases as shown in figure 11(*b*). For the $D_s = 0.5D$ case, the critical Ca_T is not reached even at a very large value ($Ca_T = 7.4$). Therefore, it is foreseen that, for a sufficiently small bubble, the cusp instability will not happen at any finite

capillary number. This tendency is consistent with the experimental observation of Liu *et al.* (1995).

7. Conclusions

Linear stability analysis is performed to predict the trailing-edge three-dimensional cusp formation for a gas bubble rising in a viscoelastic fluid. The results identify a uniquely unstable eigenmode with the azimuthal wavenumber $m = 2$ which leads to a 'knifelike' cusp. The fact that the eigenvalue corresponding to this unstable mode does not have an imaginary part indicates that the development of the three-dimensional cusp is not a Hopf-type bifurcation but an exchange of stabilities. This cusped bubble behaviour could be analogous to the collapse of an overpressurized cylindrical rubber tube in a lateral direction corresponding to the $m = 2$ mode, although a strict justification based on quantitative analysis of the latter is still needed. The mechanism of cusp instability is explored by examining the energy budget equation for perturbation terms. The analysis indicates that small disturbances are energized by base-flow energy transport via the triple interaction among the base-state pressure gradient ($\partial \bar{P}/\partial \bar{n}$), the normal displacement perturbation (H_n') and the normal velocity perturbation (u_n') on the free surface. This combination can be interpreted as the p–V work done by the base pressure on the perturbed volume. The role of viscoelasticity is implicit. Viscoelastic effects play an important role in setting up the base-state pressure gradient which can then drive the three-dimensional instability of the cusp. The results also demonstrate that, for a fixed Deborah number, there exist a critical bubble size and a capillary number beyond which the asymmetric cusp is likely to form. These predictions are consistent with experimental observations.

This work was supported by NASA Grant NAG3-2760 with Dr R. Balasubramaniam as the technical monitor. The authors acknowledge the constructive comments from two anonymous reviewers and Professor McKinley.

Appendix. Governing equations in cylindrical coordinates

The dimensionless flow equations in cylindrical coordinates (z, r, ϕ) are

$$\frac{\partial u_z}{\partial z} + \frac{\partial u_r}{\partial r} + \frac{u_r}{r} + \frac{1}{r}\frac{\partial u_\phi}{\partial \phi} = 0,$$

$$\frac{\partial u_z}{\partial t} + u_z\frac{\partial u_z}{\partial z} + u_r\frac{\partial u_z}{\partial r} + u_\phi\frac{\partial u_z}{\partial \phi} = -\frac{\partial P}{\partial z} + \frac{1}{Re}\nabla^2 u_z + \frac{c}{Re}[\nabla\cdot\sigma^p]_z,$$

$$\frac{\partial u_r}{\partial t} + u_z\frac{\partial u_r}{\partial z} + u_r\frac{\partial u_r}{\partial r} + \frac{u_\phi}{r}\frac{\partial u_r}{\partial \phi} - \frac{u_\phi^2}{r} = -\frac{\partial P}{\partial r} + \frac{1}{Re}\left[\nabla^2 u_r - \frac{u_r}{r^2} - \frac{2}{r^2}\frac{\partial u_\phi}{\partial \phi}\right] + \frac{c}{Re}[\nabla\cdot\sigma^p]_r,$$

$$\frac{\partial u_\phi}{\partial t} + u_z\frac{\partial u_\phi}{\partial z} + u_r\frac{\partial u_\phi}{\partial r} + \frac{u_\phi}{r}\frac{\partial u_\phi}{\partial \phi} + \frac{u_\phi u_r}{r} = -\frac{1}{r}\frac{\partial P}{\partial \phi} + \frac{1}{Re}\left[\nabla^2 u_\phi - \frac{u_\phi}{r^2} + \frac{2}{r^2}\frac{\partial u_r}{\partial \phi}\right] + \frac{c}{Re}[\nabla\cdot\sigma^p]_\phi.$$

The perturbed flow equations in cylindrical coordinates are

$$\frac{\partial u_z'}{\partial z} + \frac{\partial u_r'}{\partial r} + \frac{u_r'}{r} + \frac{1}{r}\frac{\partial u_\phi'}{\partial \phi} = 0,$$

$$\frac{\partial u_z'}{\partial t}+\bar{u}_z\frac{\partial u_z'}{\partial z}+u_z'\frac{\partial \bar{u}_z}{\partial z}+u_r'\frac{\partial \bar{u}_z}{\partial r}+\bar{u}_r\frac{\partial u_z'}{\partial r}=-\frac{\partial P'}{\partial z}+\frac{1}{Re}\nabla^2 u_z'+\frac{c}{Re}[\nabla\cdot\sigma^{p\prime}]_z,$$

$$\frac{\partial u_r'}{\partial t}+\bar{u}_z\frac{\partial u_r'}{\partial z}+u_z'\frac{\partial \bar{u}_r}{\partial z}+\bar{u}_r\frac{\partial u_r'}{\partial r}+u_r'\frac{\partial \bar{u}_r}{\partial r}-\frac{u_\phi'^2}{r}=-\frac{\partial P'}{\partial r}+\frac{1}{Re}\left[\nabla^2 u_r'-\frac{u_r'}{r^2}-\frac{2}{r^2}\frac{\partial u_\phi'}{\partial \phi}\right]+\frac{c}{Re}[\nabla\cdot\sigma^{p\prime}]_r,$$

$$\frac{\partial u_\phi'}{\partial t}+\bar{u}_z\frac{\partial u_\phi'}{\partial z}+u_z'\frac{\partial \bar{u}_\phi}{\partial z}+\bar{u}_r\frac{\partial u_\phi'}{\partial r}+\frac{u_\phi'\bar{u}_r}{r}=-\frac{1}{r}\frac{\partial P'}{\partial \phi}+\frac{1}{Re}\left[\nabla^2 u_\phi'-\frac{u_\phi'}{r^2}+\frac{2}{r^2}\frac{\partial u_r'}{\partial \phi}\right]+\frac{c}{Re}[\nabla\cdot\sigma^{p\prime}]_\phi,$$

where

$$[\nabla\cdot\sigma^{p\prime}]_z=\frac{\partial \sigma_{zz}^{p\prime}}{\partial z}+\frac{\partial \sigma_{zr}^{p\prime}}{\partial r}+\frac{\sigma_{zr}^{p\prime}}{r}+\frac{1}{r}\frac{\partial \sigma_{z\phi}^{p\prime}}{\partial \phi},$$

$$[\nabla\cdot\sigma^{p\prime}]_r=\frac{\partial \sigma_{zr}^{p\prime}}{\partial z}+\frac{\partial \sigma_{rr}^{p\prime}}{\partial r}+\frac{\sigma_{rr}^{p\prime}}{r}+\frac{1}{r}\frac{\partial \sigma_{r\phi}^{p\prime}}{\partial \phi}-\frac{\sigma_{\phi\phi}^{p\prime}}{r},$$

$$[\nabla\cdot\sigma^{p\prime}]_\phi=\frac{\partial \sigma_{z\phi}^{p\prime}}{\partial z}+\frac{\partial \sigma_{r\phi}^{p\prime}}{\partial r}+\frac{2\sigma_{r\phi}^{p\prime}}{r}+\frac{1}{r}\frac{\partial \sigma_{\phi\phi}^{p\prime}}{\partial \phi}.$$

The dimensionless FENE-CR constitutive equations in cylindrical coordinates are

$$\frac{f(R)A_{zz}}{De}+\frac{\partial A_{zz}}{\partial t}+(\boldsymbol{u}\cdot\nabla)A_{zz}-2\left(A_{zr}\frac{\partial u_z}{\partial r}+\frac{A_{z\phi}}{r}\frac{\partial u_z}{\partial \phi}+A_{zz}\frac{\partial u_z}{\partial z}\right)=2\frac{\partial u_z}{\partial z},$$

$$\frac{f(R)A_{rr}}{De}+\frac{\partial A_{rr}}{\partial t}+(\boldsymbol{u}\cdot\nabla)A_{rr}-\frac{u_\phi}{r}(2A_{r\phi})-2\left[A_{rr}\frac{\partial u_r}{\partial r}+A_{r\phi}\left(\frac{1}{r}\frac{\partial u_r}{\partial \phi}-\frac{u_\phi}{r}\right)+A_{zr}\frac{\partial u_r}{\partial z}\right]=2\frac{\partial u_r}{\partial r},$$

$$\frac{f(R)A_{zr}}{De}+\frac{\partial A_{zr}}{\partial t}+(\boldsymbol{u}\cdot\nabla)A_{zr}-\frac{u_\phi}{r}(2A_{z\phi})-\left[A_{zr}\frac{\partial u_r}{\partial r}+A_{z\phi}\left(\frac{1}{r}\frac{\partial u_r}{\partial \phi}-\frac{u_\phi}{r}\right)+A_{zz}\frac{\partial u_r}{\partial z}\right]$$
$$-\left[A_{zr}\frac{\partial u_z}{\partial z}+A_{r\phi}\left(\frac{1}{r}\frac{\partial u_z}{\partial \phi}\right)+A_{rr}\frac{\partial u_z}{\partial z}\right]=\left(\frac{\partial u_z}{\partial r}+\frac{\partial u_r}{\partial z}\right),$$

$$\frac{f(R)A_{\phi\phi}}{De}+\frac{\partial A_{\phi\phi}}{\partial t}+(\boldsymbol{u}\cdot\nabla)A_{\phi\phi}-\frac{u_\phi}{r}(2A_{r\phi})-2\left[A_{r\phi}\frac{\partial u_\phi}{\partial r}+A_{\phi\phi}\left(\frac{1}{r}\frac{\partial u_\phi}{\partial \phi}+\frac{u_r}{r}\right)\right.$$
$$\left.+A_{z\phi}\frac{\partial u_\phi}{\partial z}\right]=2\left(\frac{1}{r}\frac{\partial u_\phi}{\partial \phi}+\frac{u_r}{r}\right),$$

$$\frac{f(R)A_{z\phi}}{De}+\frac{\partial A_{z\phi}}{\partial t}+(\boldsymbol{u}\cdot\nabla)A_{z\phi}+\frac{u_\phi}{r}A_{zr}-\left[A_{zr}\frac{\partial u_\phi}{\partial r}+A_{z\phi}\left(\frac{1}{r}\frac{\partial u_\phi}{\partial \phi}+\frac{u_r}{r}\right)+A_{zz}\frac{\partial u_\phi}{\partial z}\right]$$
$$-\left[A_{z\phi}\frac{\partial u_z}{\partial z}+A_{\phi\phi}\frac{1}{r}\frac{\partial u_z}{\partial \phi}+A_{r\phi}\frac{\partial u_z}{\partial r}\right]=\left(\frac{\partial u_\phi}{\partial z}+\frac{1}{r}\frac{\partial u_z}{\partial \phi}\right),$$

$$\frac{f(R)A_{r\phi}}{De}+\frac{\partial A_{r\phi}}{\partial t}+(\boldsymbol{u}\cdot\nabla)A_{r\phi}+\frac{u_\phi}{r}(A_{rr}-A_{\phi\phi})-\left[A_{rr}\frac{\partial u_\phi}{\partial r}+A_{r\phi}\left(\frac{1}{r}\frac{\partial u_\phi}{\partial \phi}+\frac{u_r}{r}\right)\right.$$
$$\left.+A_{zr}\frac{\partial u_\phi}{\partial z}\right]-\left[A_{r\phi}\frac{\partial u_r}{\partial r}+A_{\phi\phi}\left(\frac{1}{r}\frac{\partial u_r}{\partial \phi}-\frac{u_\phi}{r}\right)+A_{z\phi}\frac{\partial u_r}{\partial z}\right]=\left(\frac{\partial u_\phi}{\partial r}+\frac{1}{r}\frac{\partial u_r}{\partial \phi}-\frac{u_\phi}{r}\right).$$

The perturbed FENE-CR constitutive equations in cylindrical coordinates are

$$\frac{f(\bar{R})A'_{zz}}{De}+\frac{f(R)'\bar{A}_{zz}}{De}+\frac{\partial A'_{zz}}{\partial t}+(\bar{\boldsymbol{u}}\cdot\nabla)A'_{zz}+(\boldsymbol{u}'\cdot\nabla)\bar{A}_{zz}-2\left(A'_{zr}\frac{\partial\bar{u}_z}{\partial r}+\bar{A}_{zr}\frac{\partial u'_z}{\partial r}+\bar{A}_{zz}\frac{\partial u'_z}{\partial z}+A'_{zz}\frac{\partial\bar{u}_z}{\partial z}\right)=2\frac{\partial u'_z}{\partial z},$$

$$\frac{f(\bar{R})A'_{rr}}{De}+\frac{f(R)'\bar{A}_{rr}}{De}+\frac{\partial A'_{rr}}{\partial t}+(\bar{\boldsymbol{u}}\cdot\nabla)A'_{rr}+(\boldsymbol{u}'\cdot\nabla)\bar{A}_{rr}-2\left[\bar{A}_{rr}\frac{\partial u'_r}{\partial r}+A'_{rr}\frac{\partial\bar{u}_r}{\partial r}+\bar{A}_{zr}\frac{\partial u'_r}{\partial z}+A'_{zr}\frac{\partial\bar{u}_r}{\partial z}\right]=2\frac{\partial u'_r}{\partial r},$$

$$\frac{f(\bar{R})A'_{zr}}{De}+\frac{f(R)'\bar{A}_{zr}}{De}+\frac{\partial A'_{zr}}{\partial t}+(\bar{\boldsymbol{u}}\cdot\nabla)A'_{zr}+(\boldsymbol{u}'\cdot\nabla)\bar{A}_{zr}-\left[\bar{A}_{zr}\frac{\partial u'_r}{\partial r}+A'_{zr}\frac{\partial\bar{u}_r}{\partial r}+\bar{A}_{zz}\frac{\partial u'_r}{\partial z}+A'_{zz}\frac{\partial\bar{u}_r}{\partial z}\right]-\left[\bar{A}_{zr}\frac{\partial u'_z}{\partial z}+A'_{zr}\frac{\partial\bar{u}_z}{\partial z}+\bar{A}_{rr}\frac{\partial u'_z}{\partial z}+A'_{rr}\frac{\partial\bar{u}_z}{\partial z}\right]=\left(\frac{\partial u'_z}{\partial r}+\frac{\partial u'_r}{\partial z}\right),$$

$$\frac{f(\bar{R})A'_{\phi\phi}}{De}+\frac{f(R)'\bar{A}_{\phi\phi}}{De}+\frac{\partial A'_{\phi\phi}}{\partial t}+(\bar{\boldsymbol{u}}\cdot\nabla)A'_{\phi\phi}+(\boldsymbol{u}'\cdot\nabla)\bar{A}_{\phi\phi}-2\left[\bar{A}_{\phi\phi}\left(\frac{1}{r}\frac{\partial u'_\phi}{\partial\phi}+\frac{u'_r}{r}\right)+A'_{\phi\phi}\left(\frac{\bar{u}_r}{r}\right)\right]=2\left(\frac{1}{r}\frac{\partial u'_\phi}{\partial\phi}+\frac{u'_r}{r}\right),$$

$$\frac{f(\bar{R})A'_{z\phi}}{De}+\frac{f(R)'\bar{A}_{z\phi}}{De}+\frac{\partial A'_{z\phi}}{\partial t}+(\bar{\boldsymbol{u}}\cdot\nabla)A'_{z\phi}+\frac{u'_\phi}{r}\bar{A}_{zr}-\left[\bar{A}_{zr}\frac{\partial u'_\phi}{\partial r}+A'_{z\phi}\left(\frac{\bar{u}_r}{r}\right)+\bar{A}_{zz}\frac{\partial u'_\phi}{\partial z}\right]-\left[A'_{z\phi}\frac{\partial\bar{u}_z}{\partial z}+\bar{A}_{\phi\phi}\frac{1}{r}\frac{\partial u'_z}{\partial\phi}+A'_{r\phi}\frac{\partial\bar{u}_z}{\partial r}\right]=\left(\frac{\partial u'_\phi}{\partial z}+\frac{1}{r}\frac{\partial u'_z}{\partial\phi}\right),$$

$$\frac{f(\bar{R})A'_{r\phi}}{De}+\frac{f(R)'\bar{A}_{r\phi}}{De}+\frac{\partial A'_{r\phi}}{\partial t}+(\bar{\boldsymbol{u}}\cdot\nabla)A'_{r\phi}+\frac{u'_\phi}{r}(\bar{A}_{rr}-\bar{A}_{\phi\phi})-\left[\bar{A}_{rr}\frac{\partial u'_\phi}{\partial r}+A'_{r\phi}\left(\frac{\bar{u}_r}{r}\right)+\bar{A}_{zr}\frac{\partial u'_\phi}{\partial z}\right]-\left[A'_{r\phi}\frac{\partial\bar{u}_r}{\partial r}+\bar{A}_{\phi\phi}\left(\frac{1}{r}\frac{\partial u'_r}{\partial\phi}-\frac{u'_\phi}{r}\right)+A'_{z\phi}\frac{\partial\bar{u}_r}{\partial z}\right]=\left(\frac{\partial u'_\phi}{\partial r}+\frac{1}{r}\frac{\partial u'_r}{\partial\phi}-\frac{u'_\phi}{r}\right),$$

where

$$\bar{\boldsymbol{u}}\cdot\nabla=\bar{u}_r\frac{\partial}{\partial r}+\bar{u}_z\frac{\partial}{\partial z},$$

$$\boldsymbol{u}'\cdot\nabla=u'_r\frac{\partial}{\partial r}+u'_z\frac{\partial}{\partial z}+\frac{u'_\phi}{r}\frac{\partial}{\partial\phi}.$$

REFERENCES

Batchelor, G. K. & Gill, A. E. 1962 Analysis of the stability of axisymmetric jets. *J. Fluid Mech.* **14**, 529–551.

Belmonte, A. 2000 Self-oscillations of a cusped bubble rising through a micellar solution. *Rheol. Acta* **39**, 554–559.

Chilcott, M. D. & Rallison, J. M. 1988 Creeping flow of dilute polymer solutions past cylinders and spheres. *J. Non-Newton. Fluid Mech.* **29**, 381–432.

Chorin, A. 1967 A numerical method for solving incompressible viscous flow problems. *J. Comput. Phys.* **2** (1), 12–26.

Hassager, O. 1979 Negative wake behind bubbles in non-Newtonian liquids. *Nature* **279**, 402–403.

Khorrami, M. R., Malik, M. R. & Ash, R. L. 1989 Application of spectral collocation techniques to the stability of swirling flows. *J. Comput. Phys.* **81**, 206–229.

Kim, I. & Pearlstein, A. J. 1990 Stability of the flow past a sphere. *J. Fluid Mech.* **211**, 73–93.

Kuhlmann, H. C. & Rath, H. J. 1993 Hydrodynamic instabilities in cylindrical thermocapillary liquid bridges. *J. Fluid Mech.* **247**, 247–274.

Lehoucq, R. B., Sorensen, D. C. & Yang, C. 1998 *ARPACK Users' Guide: Solution of Large Scale Eigenvalue Problems with Implicitly Restarted Arnoldi Methods*, SIAM series in software, environments and tools. SIAM.

Levenstam, M., Amberg, G. & Winkler, C. 2001 Instabilities of thermocapillary convection in a half-zone at intermediate Prandtl numbers. *Phys. Fluids* **13** (4), 807–816.

Liu, Y. J., Liao, T. Y. & Joseph, D. D. 1995 A two-dimensional cusp at the trailing edge of an air bubble rising in a viscoelastic liquid. *J. Fluid Mech.* **304**, 321–342.

Ramanan, N. & Homsy, G. M. 1994 Linear stability of lid-driven cavity flow. *Phys. Fluids* **6**, 2690–2701.

Roe, P. L. 1981 Approximate riemann solvers, parameter vectors, and difference schemes. *J. Comput. Phys.* **43**, 357–372.

Sorensen, D. C. 1992 Implicit application of polynomial filters in a k-step Arnoldi method. *SIAM J. Matrix Anal. App.* **13** (1), 357–385.

You, R., Borhan, A. & Haj-Hariri, H. 2008 A finite volume formulation for simulating drop motion in a viscoelastic two-phase system. *J. Non-Newton. Fluid Mech.* **153**, 109–129.

Zebib, A. 1987 Removal of spurious modes encountered in solving stability problems by spectral methods. *J. Comput. Phys.* **70**, 521–525.